Supplementary Information (SI) for Journal of Materials Chemistry A.
This journal is © The Royal Society of Chemistry 2025

Supplementary Information

Synergistic Fe,Pd diatomic sites anchored on porous nitrogen-doped carbon for efficient oxygen reduction in the entire pH range

Yejung Choi[a,b,†], Byoung Joon Park[c,†], Yechan Lee[b], Kug-Seung Lee[d,], Jin Kon Kim[a,b,*], and Jeong Woo Han[c,*]*

[a]National Creative Research Initiative Center for Hybrid Nano Materials by High-level Architectural Design of Block Copolymer

[b]Department of Chemical Engineering, Pohang University of Science and Technology (POSTECH), Pohang, Gyeongbuk 37673, Republic of Korea

[c]Department of Materials Science and Engineering, Research Institute of Advanced Materials, Seoul National University, Seoul 08826, Republic of Korea

[d]Beamline Division, Pohang Accelerator Laboratory, Pohang, Gyeongbuk 37673, Republic of Korea

[†]These authors contributed equally to this work

[*]Corresponding Authors. E-mail: lks3006@postech.ac.kr (K.-S.L), jkkim@postech.ac.kr (J.K.K), jwhan98@snu.ac.kr (J.W.H)

Experimental section

Chemical reagents

All chemicals were purchased from Sigma-Aldrich and used without further purification. Carbon paper (Sigracet 22 BB) was obtained from Fuel Cell Store, Germany. Zinc foil and nickel foam were sourced from Thermo Fisher Scientific Inc., USA.

Preparation of Fe,Pd-NC catalyst

The Fe,Pd-NC catalyst was synthesized using the following procedure. First, 0.59 g of $Zn(NO_3)_2 \cdot 6H_2O$ and 0.032 g $PdCl_2$ were dissolved in a mixture of 10 mL methanol and 20 mL dimethylformamide to form solution A. Separately, 1.64 g of 2-methylimidazole was dissolved in 20 mL methanol to form solution B. Solution A was then added to solution B, and the mixture was stirred at room temperature for 20 hours to obtain Pd-ZIF-8 precursors. The resulting product was washed three times with methanol, dried in a vacuum oven, and physically mixed with NaCl at a Pd-ZIF-8:NaCl weight ratio of 1:1. The mixture was then pyrolyzed at 900 °C in an argon environment for 2 hours at a heating rate of 5 °C/min. Afterwards, residual NaCl was removed with deionized water, yielding porous Fe,Pd-NC. Next, 0.1 g of the porous Pd-NC was dispersed in 60 mL of methanol containing 4.1 mg of $Fe(NO_3)_3 \cdot 9H_2O$ and stirred for 6 hours. The product was washed with methanol to remove unanchored Fe ions, collected by centrifugation, and subjected to a second pyrolysis step at 900 ^oC for 2 hours in argon atmosphere. For comparison, Fe-NC and Pd-NC catalysts were synthesized using the same procedure, by similar procedure without the addition of Pd and Fe metals, respectively.

Materials Characterization

The morphology of the catalysts was examined using a field-emission scanning electron microscope (FE-SEM) (S-4800, Hitachi, Japan) and a high-resolution transmission electron microscope (HR-TEM) (JEM-2200FS, JEOL, Japan) equipped with an image spherical aberration corrector. High-angle annular dark-field scanning transmission electron microscope (HAADF-STEM) images were obtained using a STEM (ARM 200F, JEOL, Japan) at the Materials Imaging & Analysis Center of POSTECH, South Korea. The surface area and pore size distribution were determined by N_2 adsorption measurements using the Brunauer–Emmett–Teller (BET) method (BELSORP-mini II, MicrotracBEL, Japan). The degree of structural disorder in the carbon supports was analyzed via Raman spectroscopy (Ram II-Senterra, Bruker, USA). Crystal structures were identified using X-ray diffraction (XRD, D/MAX-2500/PC, Rigaku, Japan). The chemical states and elemental compositions were characterized by XPS (Vgescalab 250, Thermo Fisher Scientific, USA) with a monochromatic Al-Kα radiation source (hν = 1486.9 eV). Metal content analysis was performed using inductively coupled plasma-atomic emission spectroscopy (ICP-AES, Spectro ARCOS EOP, Spectro, Germany). XAFS measurements were conducted at the 8C nanoprobe XAFS beamline (BL8C) of the Pohang Light Source (PLS-II) in a 3.0 GeV storage ring with a ring current of 250 mA. The X-ray beam was monochromated using a Si(111) double crystal, reducing beam intensity by 30% to suppress higher-order harmonics. The beam was then directed to a secondary source aperture and adjusted to a size of 0.5 mm (v) × 1 mm (h). XAFS spectra were collected in transmission mode and processed using the Demeter package. Extended X-ray absorption fine structure (EXAFS) spectra were fitted in the Fourier-transform range of 3.5–12 $Å^{-1}$ with a Hanning window applied between 1.2 Å and 5.3 Å. The amplitude reduction factor (S_o^2) was set to 0.8, and wavelet transform analysis was performed using $\sigma = 1$ and $\eta = 5$.

Electrochemical measurements

Electrochemical measurements were conducted using a PGSTAT302N type potentiostat/galvanostat in a three-electrode system. The working electrode was prepared by dispersing 10 mg of catalyst in a mixture of 100 μL deionized water, 400 μL ethanol, and 100 μL Nafion solution (5 wt.%). The catalyst ink was sonicated for 1 hour to ensure uniform dispersion. Subsequently, 7 μL of the ink was drop cast onto a glassy carbon rotating disk electrode (RDE) with a surface area of 0.196 cm^2, achieving a catalyst mass loading of 0.6 mg/cm^2. A saturated calomel electrode and a Pt plate were used as the reference and counter electrodes, respectively. Catalytic performance tests were carried out in 0.1 M KOH (alkaline), 0.1 M PBS (neutral), and 0.1 M $HClO_4$ (acidic) electrolytes. Before measurements, the electrolyte was purged with O_2 for 30 minutes to ensure O_2 saturation. Linear sweep voltammetry (LSV) was performed in an O_2-saturated electrolyte at a scan rate of 5 mV/s with electrode rotation speeds ranging from 800 to 2400 rpm. The electron transfer number (*n*) and kinetic current density (j_k) were determined using the Koutecky-Levich (K-L) equation [1,2]:

$$J^{-1} = J_L^{-1} + J_K^{-1} = B^{-1}\omega^{-1} + J_K^{-1} \#(1)$$

$$B = 0.62nFC_0D_0^{\frac{2}{3}}v^{-\frac{1}{6}} \#(2)$$

$$J_K = nFkC_0 \#(3)$$

where J is the measured current density, J_L is the diffusion-limiting current density, J_K is the kinetic current density, ω is the electrode rotation speed, F is the Faraday constant (96485 C mol^{-1}), C_0 is the dissolved O_2 concentration (1.2×10^{-6} mol cm^{-3}), D_0 is the diffusion coefficient of O_2 (1.9×10^{-5} cm^2 s^{-1}), v is the kinetic viscosity of 0.1 M KOH (0.01 cm^2 s^{-1}), and k is the electron transfer rate constant.

Durability and methanol tolerance tests were carried out through chronoamperometry measurements at 0.7 V (vs. RHE) in O_2-saturated electrolytes, with an electrode rotation speed of 1600 rpm. Accelerated durability tests were conducted by cycling the potential between 0.7 V and 1.2 V (vs. RHE) at a scan rate of 100 mV/s for 10,000 cycles. The electrochemical double-layer capacitance (C_{dl}) was determined from cyclic voltammetry (CV) measurements in the potential range of 1.0–1.1 V (vs. RHE) at scan rates of 10, 15, 20, 25, and 30 mV/s. The electrochemically active surface area (ECSA) was then calculated using the following equation:

$$ECSA = C_{dl}/\ C_s \#(4)$$

where C_s is the average specific capacitance of a flat standard electrode with 1 cm^2 of real surface area (0.04 mF cm^{-2}).

Rotating ring-disk electrode (RRDE) tests were conducted to determine H_2O_2 yield, with the ring electrode held at a constant potential of 1.2 V (vs. RHE). The yield of H_2O_2 and the electron transfer number (n) were calculated using the following equations:

$$H_2O_2\,(\%) = 200\ \times \frac{\frac{I_R}{N}}{I_D + \frac{I_R}{N}} \#(5)$$

$$n = \ 4\ \times \frac{I_D}{I_D + \frac{I_R}{N}} \#(6)$$

where I_D is the disk current, I_R is the ring current, and N is the collection efficiency (0.26 in this work).

Hydrogen peroxide reduction reaction (HPRR) measurements were performed by obtaining LSV curves in Ar-saturated electrolytes containing 3.5 mM H_2O_2.

Fenton-like reactivity measurements

The synthesized Fe,Pd-NC and Fe-NC catalysts were dispersed in 10 mL of electrolyte solution (either 0.1 M $HClO_4$ or 0.1 M KOH) and ultrasonicated to achieve a homogeneous suspension with a concentration of 40 μg mL^{-1}. Subsequently, predetermined amounts of 2,20-azinobis (3-ethylbenzthiazoline-6-sulfonate) (ABTS) and H_2O_2 were introduced to reach final concentrations of 2 mM and 20 mM, respectively. After allowing the reaction to proceed for 7 minutes, the solution was centrifuged, and the supernatant was diluted with electrolyte at a ratio of 3:100. The resulting solution was analyzed using a UV-vis spectrophotometer (UV-1900i, Shimadzu, Japan). The production of reactive oxygen species (ROS) was quantified by monitoring the absorbance change at 417 nm.

DFT calculations

Spin-polarized density functional theory (DFT) calculations were carried out using the Vienna Ab initio Simulation Package (VASP) [3-5]. The projector augmented-wave (PAW) method was used to describe the core–valence electron interactions [6,7], and the exchange–correlation energy was treated using the generalized gradient approximation (GGA) with the Perdew–Burke–Ernzerhof (PBE) functional [8]. A plane-wave energy cutoff of 500 eV was applied, and Gaussian smearing with a width of 0.1 eV was used for electronic occupancies. Electronic self-consistency was achieved with a convergence threshold of 10^{-5} eV, and ionic relaxation was performed until the residual force on each atom was below 0.03 eV/Å. Long-range dispersion interactions were included using the DFT-D4 method [9]. Brillouin zone sampling was performed using a 3 × 3 × 1 Monkhorst–Pack k-point mesh [10]. To model single-atom Fe-NC and Pd-NC catalysts as well as dual-atom Fe,Pd–NC catalysts, a graphene supercell with dimensions of 12.33 Å × 12.83 Å, containing 60 carbon atoms, was constructed under periodic boundary conditions. To eliminate artificial interactions between periodic images, a vacuum spacing of 20 Å was introduced along the z-axis. Bader charge analysis was conducted using the grid-based Bader algorithm applied to the total charge density [11,12].

The 4-electron oxygen reduction reaction (ORR) pathway in alkaline media was modeled using the computational hydrogen electrode (CHE) approach [13]. In this framework, the free energy of each proton-coupled electron transfer (PCET) step is referenced to the standard hydrogen electrode (SHE), where the chemical potential of a proton–electron pair is equivalent to that of ½ H_2(g) under standard conditions (pH = 0, 1 bar H_2, 298 K). The ORR was assumed to proceed via the following 4-electron pathway, with adsorbed surface intermediates (* denotes an active site):

$$* + O_{2(g)} \rightarrow {}^{*}O_2\#(7)$$

$$^{*}O_2 + H_2O + e^{-} \rightarrow {}^{*}OOH + OH^{-}\#(8)$$

$$^{*}OOH + e^{-} \rightarrow {}^{*}O + OH^{-}\#(9)$$

$$^{*}O + H_2O + e^{-} \rightarrow {}^{*}OH + OH^{-}\#(10)$$

$$^{*}OH + e^{-} \rightarrow * + OH^{-}\#(11)$$

The Gibbs free energy change (ΔG) for each step was computed using the equation:

$$\Delta G = \Delta E + \Delta ZPE - T\Delta S - eU + \Delta G_{sol}\#(12)$$

where ΔE is the DFT-calculated reaction energy, ΔZPE is the zero-point energy correction, T is the temperature (298 K), ΔS is the entropy change, U is the applied potential relative to SHE, and ΔG_{sol} is a solvation correction of 0.3 eV applied to *OH and *OOH species [14].

Zinc-air battery tests

The performance of the ZAB was assessed using a custom-built ZAB setup. The air cathode was prepared by coating catalyst ink onto carbon paper with an effective area of 1.0 cm^2 and a catalyst loading of 1.0 mg cm^{-2}. The catalyst ink was formulated by dispersing 10 mg of catalyst in a solution of 0.25 mL ethanol, 0.25 mL ethylene glycol, and 0.05 mL Nafion (5 wt.%). A polished Zn foil (0.1 mm thick) was used as the anode, with nickel foam as the current collector. The electrolyte for the alkaline ZAB consisted of 6 M KOH and 0.2 M $Zn(OAc)_2$, whereas the neutral ZAB utilized an electrolyte containing 4 M NH_4Cl and 2 M KCl. All electrochemical measurements were conducted using a potentiostat (Wave Driver 10, Pine Instrument, USA). Polarization curves were recorded at a scan rate of 5 mV s^{-1} for both alkaline and neutral ZABs. Discharge tests were performed at a constant discharge current density of 20 mA cm^{-2} for the alkaline ZAB and 5 mA cm^{-2} for the neutral ZAB. The specific capacity was calculated based on the weight of the consumed Zn. Charge/discharge cycling tests were conducted in 20-minute cycles (10 minutes discharge, 10 minutes charge) at a current density of 5 mA cm^{-2} for the alkaline ZAB and 2.5 mA cm^{-2} for the neutral ZAB.

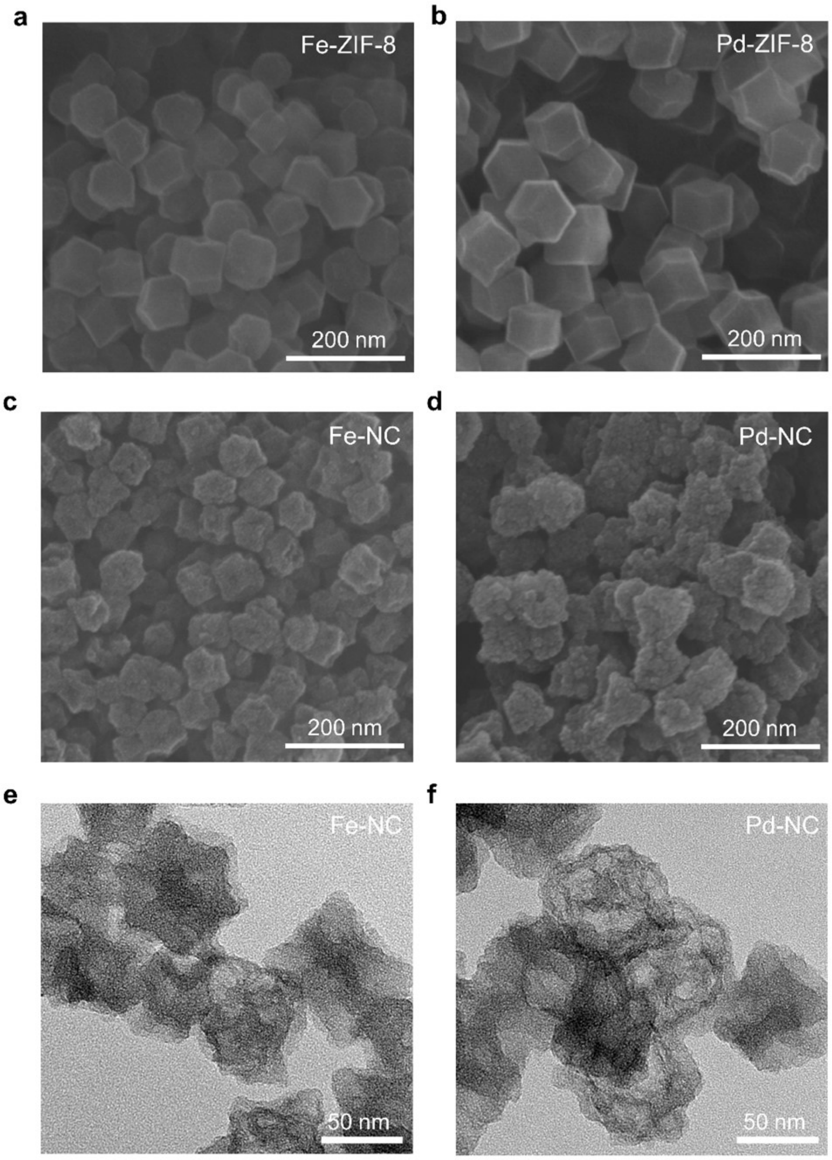

Fig. S1. FE-SEM images of (a) Fe-ZIF-8, (b) Pd-ZIF-8, (c) Fe-NC, and (d) Pd-NC. HR-TEM images of (e) Fe-NC, and (f) Pd-NC. During pyrolysis to transform M-ZIF-8 into M-NC, NaCl templates induced high porosity, while maintaining the rhombic dodecahedron structures.

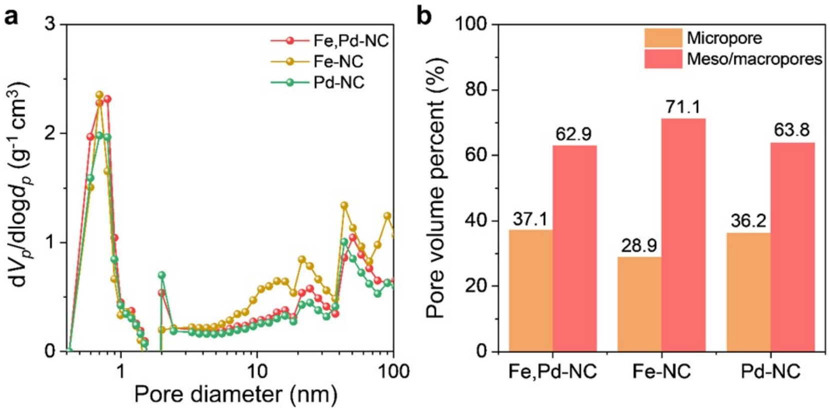

Fig. S2. (a) Pore size distribution and (b) pore volume percentages of Fe,Pd-NC, Fe-NC, and Pd-NC.

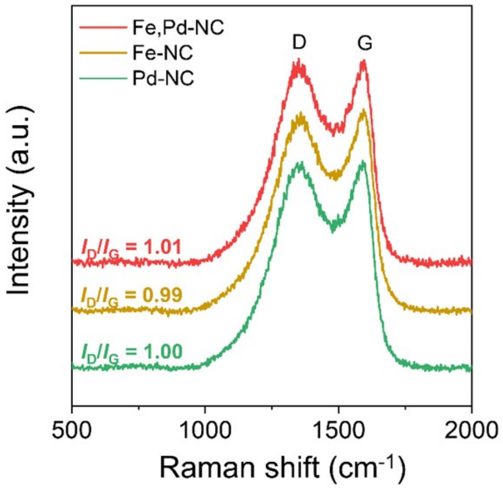

Fig. S3. Raman spectra of Fe,Pd-NC, Fe-NC, and Pd-NC.

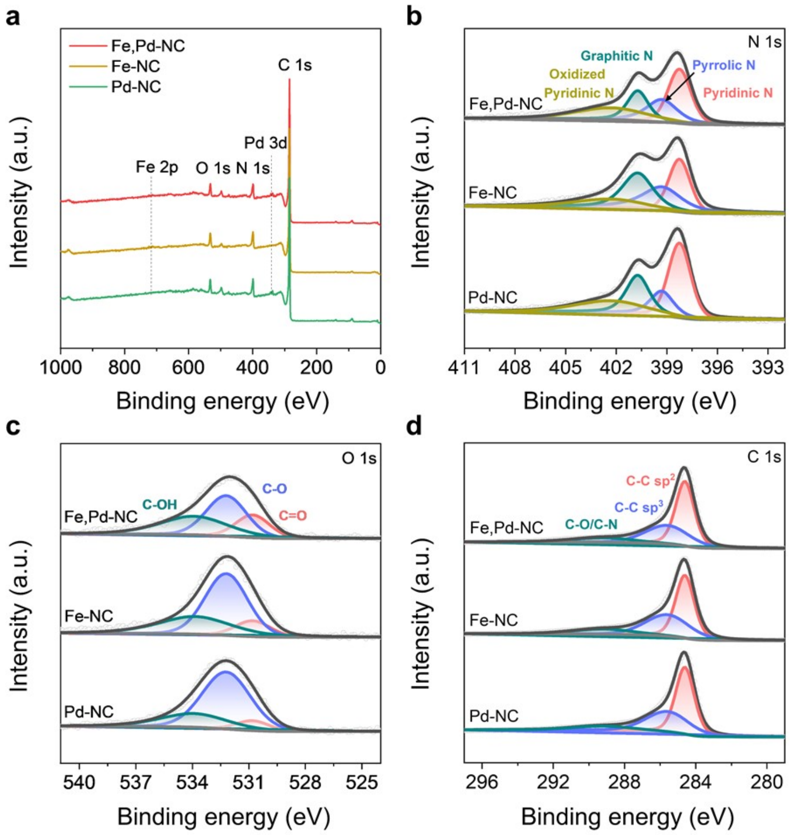

Fig. S4. (a) XPS survey spectra. (b) N 1s, (c) O 1s, and (d) C 1s XPS spectra of Fe,Pd-NC, Fe-NC, and Pd-NC.

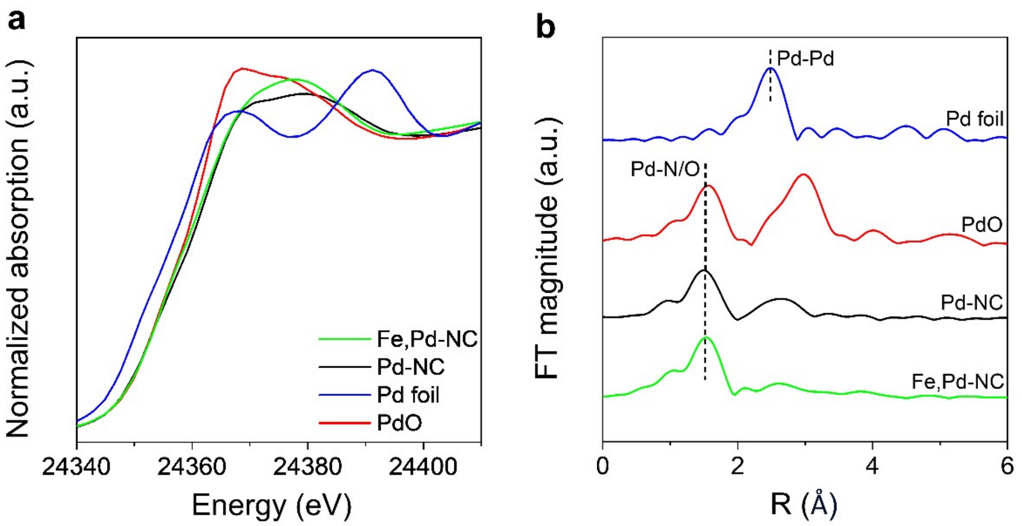

Fig. S5. (a) XANES spectra and (b) k^3-weighted FT-EXAFS spectra of Pd K-edge.

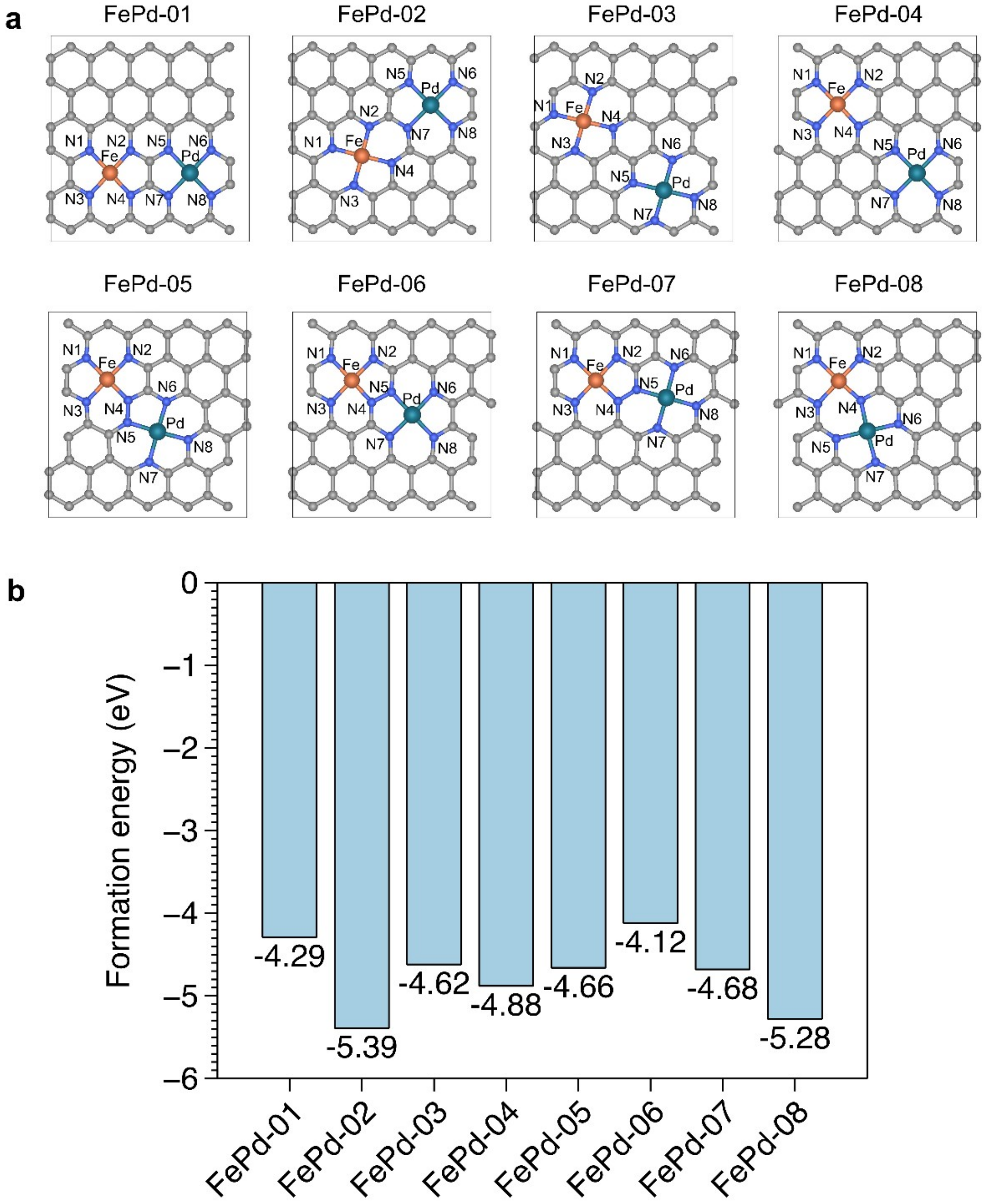

Fig. S6. (a) Constructed models for Fe,Pd dual active sites, and (b) calculated formation energy of each active site. The models in Fig. S6 were designed with interatomic distances between Fe and Pd that are not too far apart, enabling efficient LRI without direct bonding.

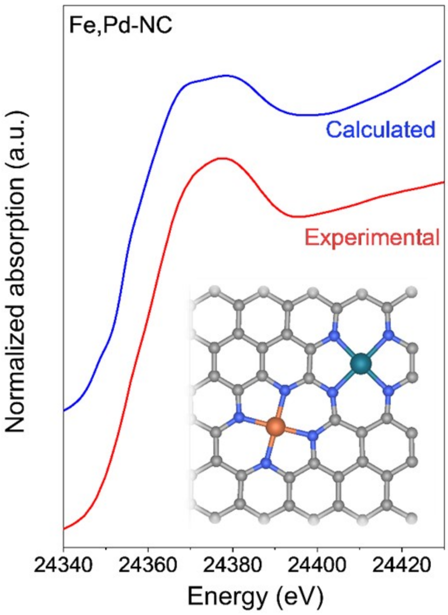

Fig. S7. Comparison of theoretically calculated and experimentally obtained Fe K-edge XANES spectra for Fe,Pd-NC catalyst.

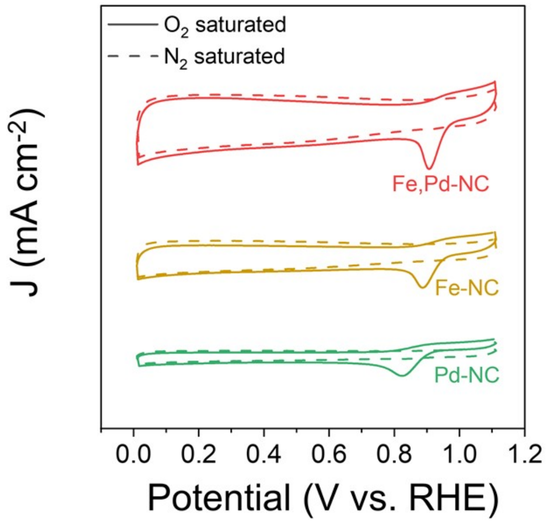

Fig. S8. CV curves of Fe,Pd-NC, Fe-NC, and Pd-NC in O_2- and N_2-saturated 0.1 M KOH solution.

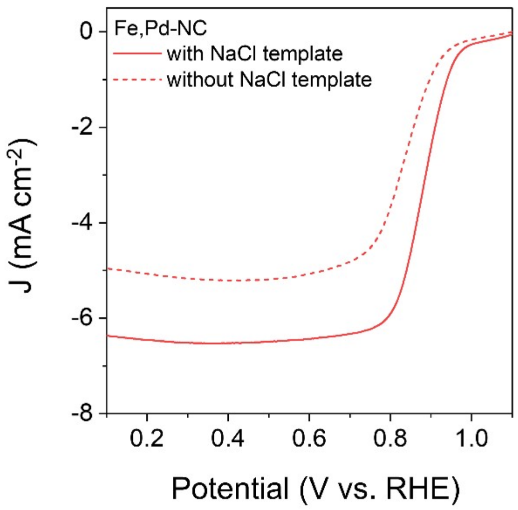

Fig. S9. LSV curves of Fe,Pd-NC prepared with and without NaCl template. The highly porous structure induced by NaCl templates results in a more positive $E_{1/2}$ of 0.884 V and a larger diffusion-limited current density of 6.38 mA cm^{-2}, compared to the non-porous structure fabricated without NaCl template ($E_{1/2}$ of 0.842 V and a limiting current density of 5.08 mA cm^{-2}).

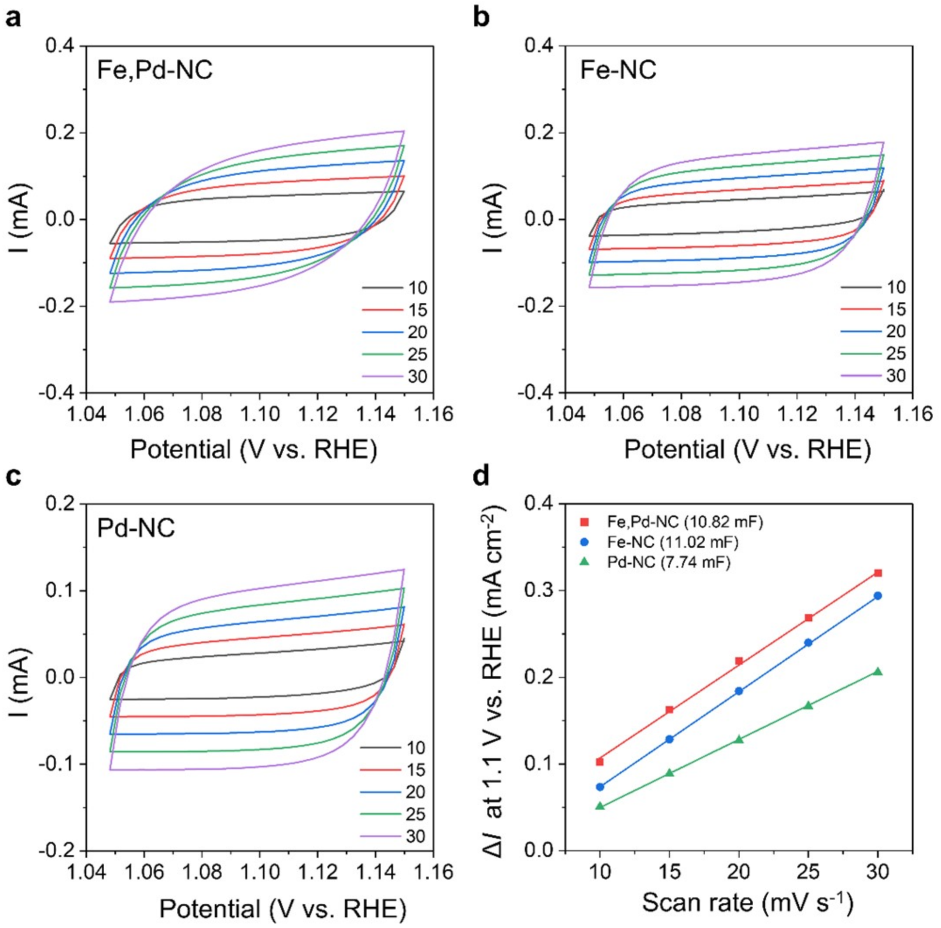

Fig. S10. CV curves of (a) Fe,Pd-NC, (b) Fe-NC, and (c) Pd-NC at various scan rates (10, 15, 20, 25, and 30 mV s^{-1}). (d) double-layer capacitance of Fe,Pd-NC, Fe-NC, and Pd-NC catalysts.

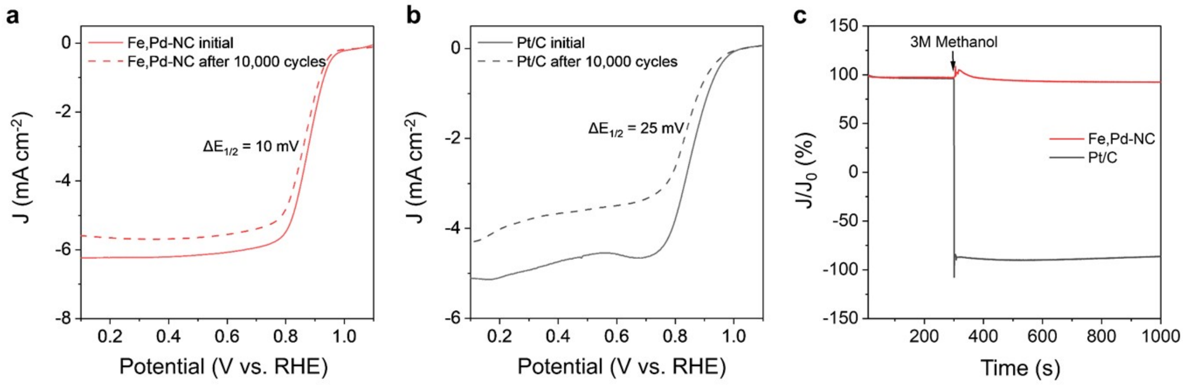

Fig. S11. Accelerated durability tests for (a) Fe,Pd-NC and (b) Pt/C. (c) Methanol tolerance tests for Fe,Pd-NC and Pt/C catalysts at 0.7 V in O_2-saturated 0.1 M KOH.

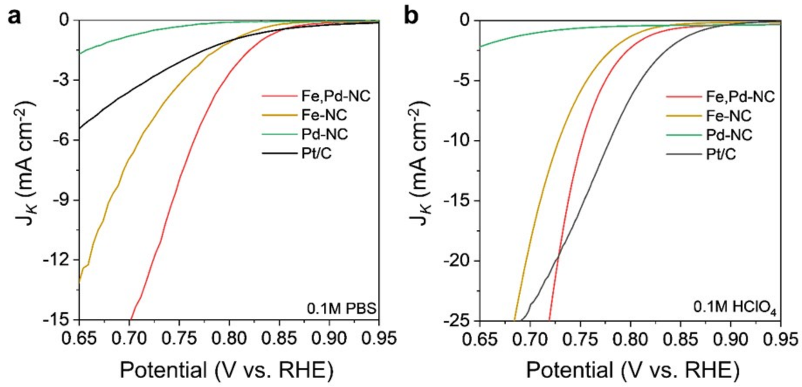

Fig. S12. Kinetic current density of prepared catalysts (Fe,Pd-NC, Fe-NC and Pd-NC) and commercial Pt/C in (a) 0.1 M PBS, and (b) 0.1 M $HClO_4$ solution.

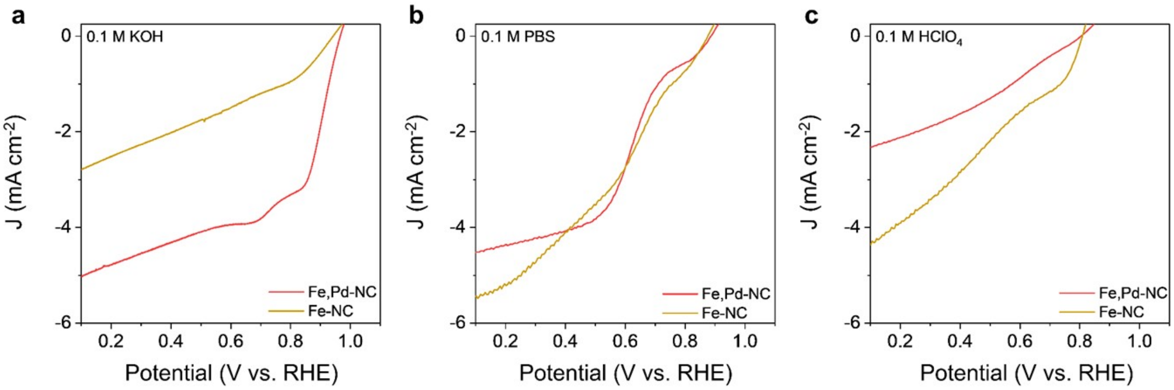

Fig. S13. H_2O_2 reduction reaction (HPRR) curves recorded in Ar-saturated 0.1 M electrolyte solutions containing 3.5 mM H_2O_2.

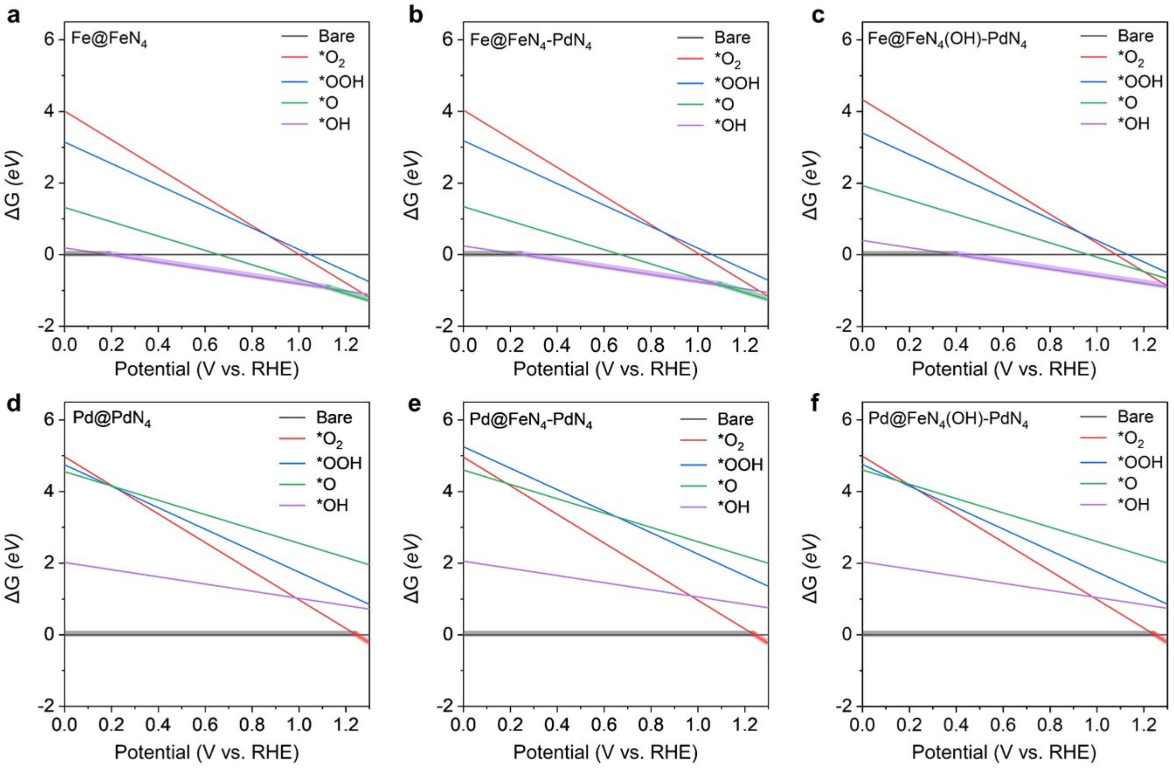

Fig. S14. Surface Pourbaix diagrams of (a-c) Fe sites: (a) FeN$_4$, (b) FeN$_4$-PdN$_4$, and (c) FeN$_4$(OH)-PdN$_4$; and (d-f) Pd sites: (d) PdN$_4$, (e) FeN$_4$-PdN$_4$, and (f) FeN$_4$(OH)-PdN$_4$. The most stable surface intermediates at each potential are highlighted in bold.

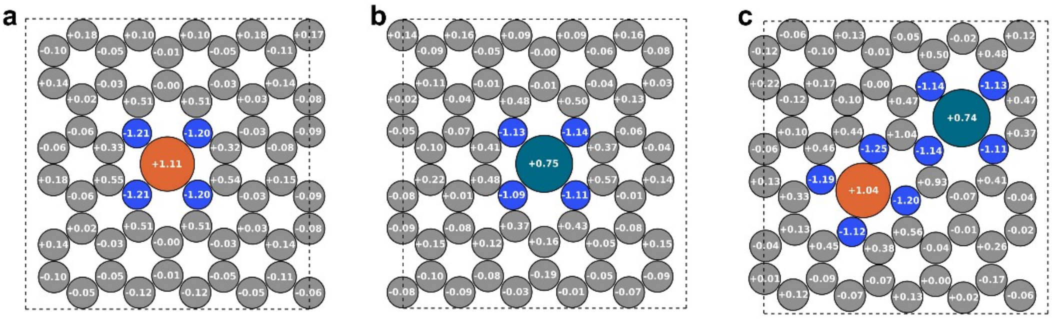

Fig. S15. Effective Bader charge results of all atoms in (a) FeN_4, (b) PdN_4 and (c) FeN_4-PdN_4

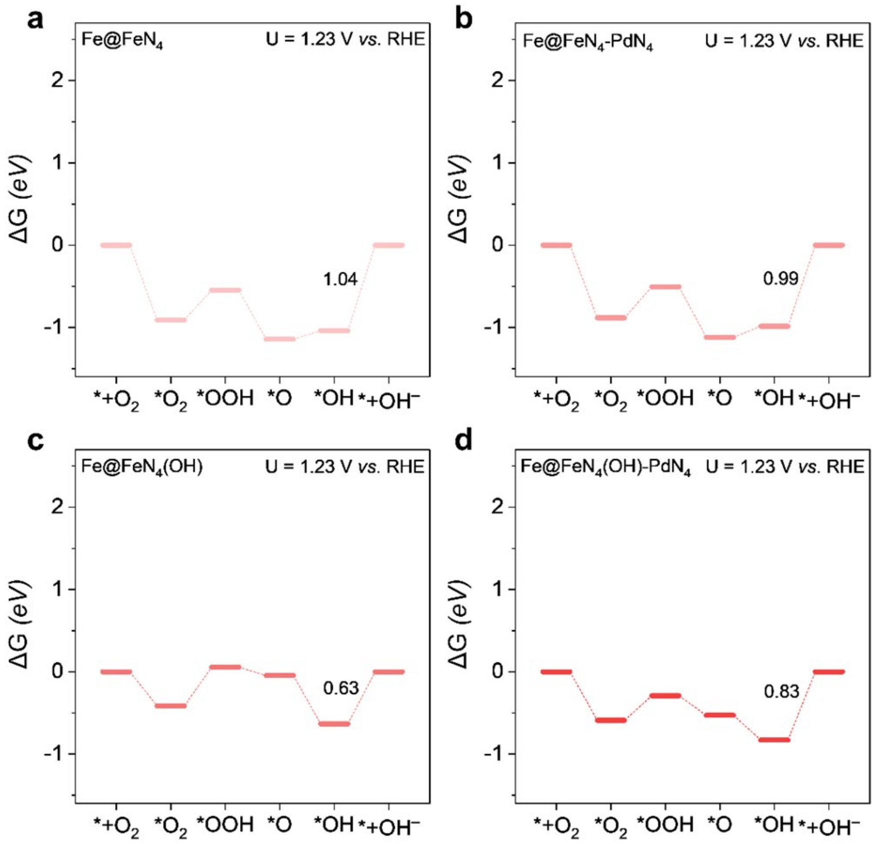

Fig. S16. Free energy diagrams for oxygen reduction reactions of Fe sites: (a) FeN$_4$, (b) FeN$_4$-PdN$_4$, (c) FeN$_4$(OH) and (d) FeN$_4$(OH)-PdN$_4$ at 1.23 V *vs*. RHE.

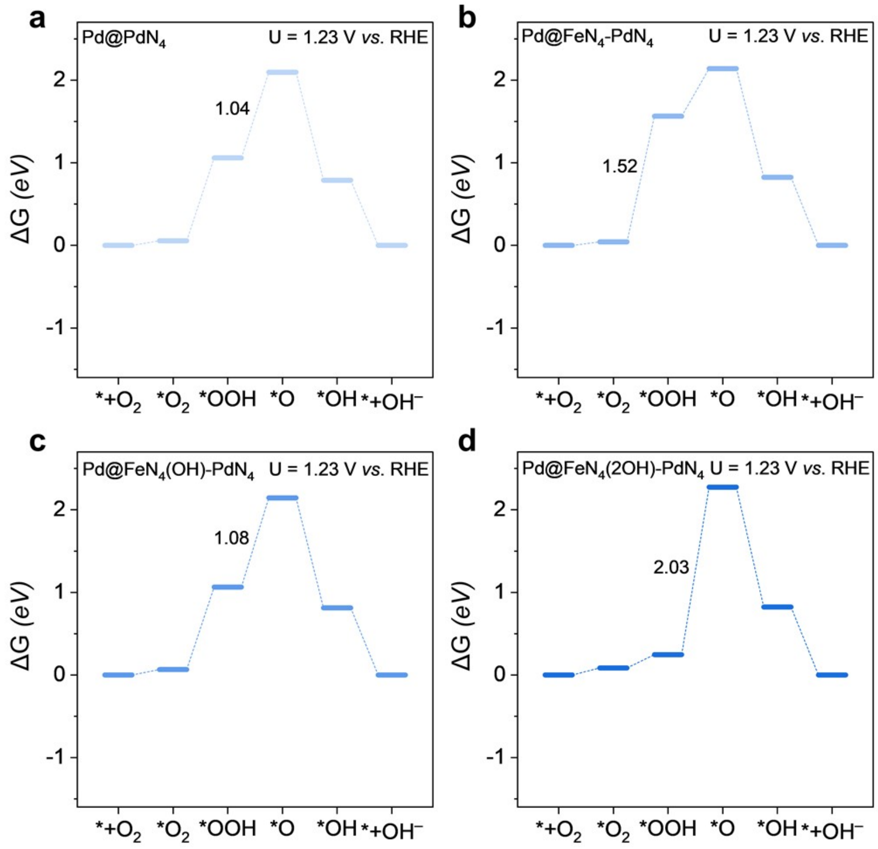

Fig. S17. Free energy diagrams for oxygen reduction reactions of Pd sites: (a) PdN$_4$, (b) FeN$_4$-PdN$_4$, (c) FeN$_4$(OH)-PdN$_4$ and (d) FeN$_4$(2OH)-PdN$_4$ at 1.23 V *vs*. RHE.

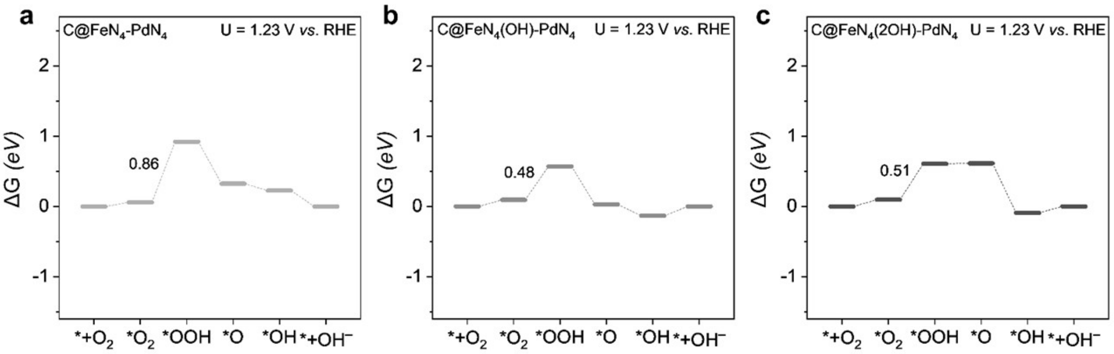

Fig. S18. Free energy diagrams for oxygen reduction reactions of C sites: (a) FeN$_4$-PdN$_4$, (b) FeN$_4$(OH)-PdN$_4$ and (c) FeN$_4$(2OH)-PdN$_4$ at 1.23 V *vs*. RHE.

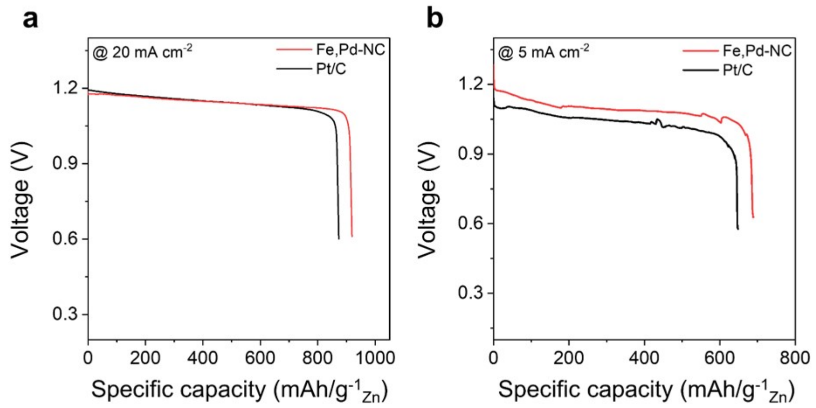

Fig. S19. Galvanostatic discharge curves of (a) alkaline ZABs at 20 mA cm^{-2}, and (b) neutral ZABs at 5 mA cm^{-2}, normalized to the weight of consumed Zn.

Table S1. BET specific surface area and pore volumes of Fe,Pd-NC, Fe-NC, and Pd-NC.

Sample	BET specific surface area [m^2 g^{-1}]	Micropore volume [cm^3 g^{-1}]	Meso/macropores volume [cm^3 g^{-1}]	Total pore Volume [cm^3 g^{-1}]
Fe,Pd-NC	1234.4	0.456	0.772	1.228
Fe-NC	1337.9	0.386	0.948	1.334
Pd-NC	1187.8	0.420	0.740	1.160

Table S2. Elemental content of Fe and Pd in Fe,Pd-NC, Fe-NC, and Pd-NC determined via ICP-AES.

Sample	Fe (wt %)	Pd (wt %)
Fe,Pd-NC	0.48	1.07
Fe-NC	0.72	—
Pd-NC	—	1.56

Table S3. Atomic composition of Fe and Pd in Fe,Pd-NC, Fe-NC, and Pd-NC determined via XPS.

Sample	Fe (at %)	Pd (at %)
Fe,Pd-NC	0.1	0.13
Fe-NC	0.17	–
Pd-NC	–	0.2

Table S4. Summary of Pd K-edge EXAFS curves fitting parameters.

(N = coordination number, R = interatomic distance, σ^2 = Debye-Waller factor (bond disorder), R-Factor = a measure of the quality of EXASFS fit.)

Sample	Edge	Path	N	R (Å)	σ^2 (Å^2)	R-factor (%)
FePd-NC	Pd K	Pd-N	2	2.005 ± 0.007	0.003 ± 0.001	1.2
		Pd-N	1	2.056 ± 0.007	0.003 ± 0.001	
		Pd-N	1	2.153 ± 0.037	0.009 ± 0.006	
		Pd-C	2	2.837 ± 0.028	0.011 ± 0.004	
		Pd-C	2	2.880 ± 0.028	0.011 ± 0.004	
		Pd-C	2	2.990 ± 0.019	0.004 ± 0.002	
		Pd-C	2	3.059 ± 0.019	0.004 ± 0.002	
		Pd-N-C	4	3.111 ± 0.022	0.007 ± 0.002	
		Pd-N-C	2	3.148 ± 0.022	0.007 ± 0.002	
		Pd-N-C	4	3.189 ± 0.013	0.004 ± 0.002	
		Pd-N	2	3.957 ± 0.014	0.006 ± 0.002	
		Pd-N	2	4.097 ± 0.014	0.006 ± 0.002	
		Pd-C-C	4	4.377 ± 0.024	0.010 ± 0.003	
		Pd-C	2	4.521 ± 0.061	0.008 ± 0.005	
		Pd-Fe	1	5.357 ± 0.046	0.006 ± 0.004	

Catalyst	0.1M KOH			0.1M PBS			0.1M $HClO_4$		
	E_{onset}	J_{k}@0.85V	$E_{1/2}$	E_{onset}	J_{k}@0.75V	$E_{1/2}$	E_{onset}	J_{k}@0.75V	$E_{1/2}$
Fe,Pd-NC	0.993	16.9	0.884	0.892	7.8	0.782	0.881	7.9	0.781
Fe-NC	0.958	4.2	0.843	0.874	3.1	0.736	0.869	4.6	0.743
Pd-NC	0.905	0.9	0.778	0.789	0.4	0.588	0.781	0.6	0.573
Pt/C	1.013	6.5	0.852	0.933	2.1	0.722	0.926	15.3	0.813

Table S5. Summary of ORR performances for the catalysts in different electrolytes.

Table S6. ECSA values for Fe,Pd-NC, Fe-NC, and Pd-NC.

Sample	Capacitance (mF)	ECSA (cm^2)
Fe,Pd-NC	10.82	270.5
Fe-NC	11.02	275.5
Pd-NC	7.74	193.5

Table S7. Comparison of ORR activity in alkaline (0.1 M KOH) electrolyte for Fe,Pd-NC and previously reported catalysts.

Catalysts	$E_{1/2}$ (V_{RHE})	References
Fe,Pd-NC	**0.884**	**This work**
Fe/Ni-N-C	0.861	15
Ni-N_4/GHSs/Fe-N_4	0.83	16
Fe_1Se_1-NC	0.88	17
FeCu-DA/NC	0.86	18
Fe_1Co_3-NC-1100	0.877	19
FeNi-NPC-1000	0.877	20
FeCo-SN-C	0.863	21
Zn/Fe-NC	0.875	22
A-SAC(Fe,Ni,Zn)/NC	0.88	23

Table S8. Comparison of ORR activity in neutral electrolyte for Fe,Pd-NC and previously reported catalysts.

Catalysts	$E_{1/2}$ (V_{RHE})	Electrolyte	References
Fe,Pd-NC	**0.782**	**0.1 M PBS**	**This work**
Fe-N-C/800-HT2	0.743	0.1 M PBS	24
NCDM-Fe-N-C-2	0.75	0.05 M PBS	25
Fe_x-N-C@TABOH	0.71	0.1 M PBS	26
1@Fe_3O_4 NR	0.57	0.1 M PBS	27
NMCS-rGO-Co	0.72	0.1 M PBS	28
Fe_{SA+NC}@NMPC	0.76	0.1 M PBS	29
Fc@Fe−NHCS	0.76	0.1 M PBS	30
FeCu-NC-0.5	0.691	0.05 M PBS	31

Table S9. Comparison of ORR activity in acidic electrolyte for Fe,Pd-NC and previously reported catalysts.

Catalysts	$E_{1/2}$ (V_{RHE})	Electrolyte	References
Fe,Pd-NC	**0.781**	**0.1 M $HClO_4$**	**This work**
FeCo-N-HCN	0.750	0.5 M H_2SO_4	32
Zn/Co-N-C	0.796	0.1 M $HClO_4$	33
FeMn-DSAC	0.790	0.5 M H_2SO_4	34
Fe,Ce-N-C	0.808	0.1 M $HClO_4$	35
Fe_1Se_1-NC	0.74	0.5 M H_2SO_4	17
Fe, Cu DAs-NC	0.80	0.5 M H_2SO_4	36
Co DAC-300	0.796	0.1 M $HClO_4$	37
CuCoNPC	0.72	0.1 M $HClO_4$	38
Fe_2@P-HC	0.75	0.1 M $HClO_4$	39
FeCo-3DMNC	0.806	0.5 M H_2SO_4	40

Table S10. Comparison of ORR activity for Fe,Pd-NC and previously reported pH-universal catalysts.

Catalysts	Alkaline $E_{1/2}$ (V_{RHE})	Neutral $E_{1/2}$ (V_{RHE})	Acidic $E_{1/2}$ (V_{RHE})	References
Fe,Pd-NC	**0.884 (0.1 M KOH)**	**0.782 (0.1 M PBS)**	**0.781 (0.1 M $HClO_4$)**	**This work**
Fe,Cu/N-C	0.86 (0.1 M KOH)	0.73 (0.1 M PBS)	0.77 (0.5 M H_2SO_4)	41
NPS-1&10&2	0.862 (0.1 M KOH)	0.712 (0.1 M PBS)	0.735 (0.1 M $HClO_4$)	42
Co-SAs/N-C/rGO	0.84 (0.1 M KOH)	0.65 (0.1 M PBS)	0.77 (0.5 M H_2SO_4)	43
FeNC-D0.5	0.866 (0.1 M KOH)	0.692 (0.05 M PBS)	0.750 (0.5 M H_2SO_4)	44
Fe-Zn-SA/NC	0.85 (0.1 M KOH)	0.72 (0.1 M PBS)	0.78 (0.1 M $HClO_4$)	45
Fe/NC-3	0.90 (1 M KOH)	0.69 (0.01 M PBS)	0.71 (0.5 M H_2SO_4)	46
γ-Fe_2O_3@CNFs-12	0.905 (0.1 M KOH)	~0.6 (0.05 M PBS)	0.692 (0.05 M H_2SO_4)	47
FeMn/NC	0.85 (0.1 M KOH)	0.65 (0.1 M NaH_2PO_4 + 0.1 M Na_2HPO_4)	0.68 (0.05 M H_2SO_4)	48
Cu_{SA}/Cu_{CT}@NPC	0.88 (0.1 M KOH)	0.74 (0.1 M PBS)	0.80 (0.1 M $HClO_4$)	49
Fe-Co-NC	0.880 (0.1 M KOH)	0.722 (0.05 M PBS)	0.729 (0.5 M H_2SO_4)	50
CA-Fe@BC	0.93 (0.1 M KOH)	0.62 (0.1 M PBS)	0.78 (0.05 M H_2SO_4)	51
Co@Fe-NC-4	0.827 (0.1 M KOH)	0.756 (0.1 M PBS)	0.674 (0.5 M H_2SO_4)	52
PT-MnN_4	0.88 (0.1 M KOH)	0.63 (0.1 M PBS)	0.73 (0.5 M H_2SO_4)	53

Table S11. Turnover frequencies (h^{-1}) of Fe,Pd-NC, Fe-NC, and Pd-NC in different electrolytes.

Catalyst	0.1M KOH (at 0.8 V)	0.1M PBS (at 0.75 V)	0.1M $HClO_4$ (at 0.75 V)
Fe,Pd-NC	9.06	0.72	0.73
Fe-NC	1.84	0.45	0.61
Pd-NC	0.35	0.05	0.07

References

1. K. Maiti, M. T. Curnan, H. J. Kim, K. Kim and J. W. Han, *J. Energy Chem.*, 2024, **93**, 669-681.
2. K.-J. Noh, H. Im, C. Lim, M. G. Jang, I. Nam and J. W. Han, *Chem. Eng. J.*, 2022, **427**, 131568.
3. G. Kresse and J. Hafner, *Phys. Rev. B*, 1993, **47**, 558.
4. G. Kresse and J. Hafner, *Phys. Rev. B*, 1994, **49**, 14251.
5. G. Kresse and J. Furthmüller, *Computational materials science*, 1996, **6**, 15-50.
6. P. E. Blöchl, *Phys. Rev. B*, 1994, **50**, 17953.
7. G. Kresse and D. Joubert, *Phys. Rev. B*, 1999, **59**, 1758.
8. J. P. Perdew, K. Burke and M. Ernzerhof, Phys. *Rev. Lett.*, 1996, **77**, 3865.
9. E. Caldeweyher, S. Ehlert, A. Hansen, H. Neugebauer, S. Spicher, C. Bannwarth and S. Grimme, *The Journal of chemical physics*, 2019, **150**.
10. H. J. Monkhorst and J. D. Pack, *Phys. Rev. B*, 1976, **13**, 5188.
11. W. Tang, E. Sanville and G. Henkelman, *J. Phys.: Condens. Matter*, 2009, **21**, 084204.
12. E. Sanville, S. D. Kenny, R. Smith and G. Henkelman, J. Comput. *Chem.*, 2007, **28**, 899-908.
13. J. K. Nørskov, J. Rossmeisl, A. Logadottir, L. Lindqvist, J. R. Kitchin, T. Bligaard and H. Jonsson, *The Journal of Physical Chemistry B*, 2004, **108**, 17886-17892.
14. J. Rossmeisl, A. Logadottir and J. K. Nørskov, *Chem. Phys.*, 2005, **319**, 178-184.

15. H. Li, J. Wang, R. Qi, Y. Hu, J. Zhang, H. Zhao, J. Zhang and Y. Zhao, *Appl. Catal. B Environ.*, 2021, **285**, 119778.

16. J. Chen, H. Li, C. Fan, Q. Meng, Y. Tang, X. Qiu, G. Fu and T. Ma, *Adv. Mater.*, 2020, **32**, 2003134.

17. Z. Chen, X. Su, J. Ding, N. Yang, W. Zuo, Q. He, Z. Wei, Q. Zhang, J. Huang and Y. Zhai, *Appl. Catal. B Environ.*, 2022, **308**, 121206.

18. C. Du, Y. Gao, H. Chen, P. Li, S. Zhu, J. Wang, Q. He and W. Chen, *J. Mater. Chem. A*, 2020, **8**, 16994-17001.

19. Y. He, X. Yang, Y. Li, L. Liu, S. Guo, C. Shu, F. Liu, Y. Liu, Q. Tan and G. Wu, *ACS catalysis*, 2022, **12**, 1216-1227.

20. Y. He, J. Yang, Y. Wang, Y. Jia, H. Li, Y. Liu, L. Liu and Q. Tan, *ACS Appl. Mater. Interfaces*, 2024, **16**, 12398-12406.

21. Z. Yang, X. Wu, G. Qin and X. Meng, *Int. J. Hydrogen Energy*, 2025, **118**, 417-425.

22. C. Fu, X. Qi, L. Zhao, T. Yang, Q. Xue, Z. Zhu, P. Xiong, J. Jiang, X. An and H. Chen, *Appl. Catal. B Environ.*, 2023, **335**, 122875.

23. J.-E. Tsai, W.-X. Hong, H. Pourzolfaghar, W.-H. Wang and Y.-Y. Li, *Chem. Eng. J.*, 2023, **460**, 141868.

24. G. Zhang, L. Li, M. Chen and F. Yang, *J. Mater. Chem. A*, 2020, **8**, 9256-9267.

25. H.-X. Liao, H.-X. Wei, S.-Q. Zhou, H.-W. Zhou, Y.-T. Cao and N. Li, *ACS Appl. Mater. Interfaces*, 2025, **8**, 4431-4440.

26. B. Jiang, N. Jiang, Y. Cui, H. Wang, G. Zhang, J. Li and Y. Zhang, *Adv. Sci.*, 2024, **11**, 2402610.

27. L. Xie, X. Li, B. Wang, J. Meng, H. Lei, W. Zhang and R. Cao, *Angew. Chem. Int. Ed.*, 2019, **58**, 18883-18887.

28. R. Xu, X. Wang, C. Zhang, Y. Zhang, H. Jiang, H. Wang, G. Su, M. Huang and A. Toghan, *Chem. Eng. J.*, 2022, **433**, 133685.

29. R. Xu, X. Wang, M. Sun, C. Zhang, C. Li, Z. Cao, M. Gu, B. Huang and M. Huang, *Chem. Eng. J.*, 2023, **475**, 146065.

30. K. Sheng, J. Li, G. Li, J. Hao, Y. Wang, Y. Liu, Y. Liu, Q. Yi and W. Li, *Appl. Surf. Sci.*, 2022, **601**, 154221.

31. L. Wu, Y. Wang, C. Shao, L. Wang and B. Li, *J. Mater. Chem. A*, 2025, **13**, 5974-5986.

32. H. Li, Y. Wen, M. Jiang, Y. Yao, H. Zhou, Z. Huang, J. Li, S. Jiao, Y. Kuang and S. Luo, *Adv. Funct. Mater.*, 2021, **31**, 2011289.

33. Z. Lu, B. Wang, Y. Hu, W. Liu, Y. Zhao, R. Yang, Z. Li, J. Luo, B. Chi and Z. Jiang, *Angew. Chem.*, 2019, **131**, 2648-2652.

34. T. Cui, Y. P. Wang, T. Ye, J. Wu, Z. Chen, J. Li, Y. Lei, D. Wang and Y. Li, *Angew. Chem. Int. Ed.*, 2022, **61**, e202115219.

35. Y. Chu, E. Luo, Y. Wei, S. Zhu, X. Wang, L. Yang, N. Gao, Y. Wang, Z. Jiang and C. Liu, *Chem Catalysis*, 2023, **3**.

36. F. Kong, M. Wang, Y. Huang, G. Meng, M. Chen, H. Tian, Y. Chen, C. Chen, Z. Chang and X. Cui, *Energy Stor. Mater.*, 2023, **54**, 533-542.

37. Q. Sun, X. Yue, L. Yu, F.-Z. Li, Y. Zheng, M.-T. Liu, J.-Z. Peng, X. Hu, H. M. Chen and L. Li, *J. Am. Chem. Soc.*, 2024, **146**, 35295-35304.

38. H. Wang, X. Zhou, J. Su, Z. Liu, B. Xiao, L. Yang, J. Wang, Y. Li, X. Lu and X. Zhu,

Chem. Eng. J., 2025, 160020.

39. Q. Miao, Z. Chen, X. Li, M. Liu, G. Liu, X. Yang, Z. Guo, C. Yu, Q. Xu and G. Zeng, *ACS Catalysis*, 2023, **13**, 11127-11135.

40. K. Chen, Y. Liang, D. Pan, J. Huang, J. Gao, Z. Lu, X. Liu, J. Chen, H. Zhang and X. Hu, *Adv. Energy Mater.*, 2025, **15**, 2404140.

41. L. Wang, Q. An, X. Sheng, Z. Mei, Q. Jing, X. Zhao, Q. Xu, L. Duan, X. Zou and H. Guo, *Appl. Catal. B Environ.*, 2024, **343**, 123509.

42. Y. Long, F. Ye, L. Shi, X. Lin, R. Paul, D. Liu and C. Hu, *Carbon*, 2021, **179**, 365-376.

43. X. Shu, D. Tan, Y. Wang, J. Ma and J. Zhang, *Angew. Chem. Int. Ed.*, 2024, **63**, e202316005.

44. S. Ji, T. Liu, L. Leng, H. Liu, J. Zhang, M. Zhang, Q. Xu, J. Zhu, M. Qiao and Y. Wang, *Appl. Catal. B Environ.*, 2023, **320**, 121987.

45. J. Xu, S. Lai, D. Qi, M. Hu, X. Peng, Y. Liu, W. Liu, G. Hu, H. Xu and F. Li, *Nano Research*, 2021, **14**, 1374-1381.

46. M. Liu, J. Lee, T. C. Yang, F. Zheng, J. Zhao, C. M. Yang and L. Y. S. Lee, *Small Methods*, 2021, **5**, 2001165.

47. Z. Yao, Y. Li, D. Chen, Y. Zhang, X. Bao, J. Wang and Q. Zhong, *Chem. Eng. J.*, 2021, **415**, 129033.

48. X. Sheng, Z. Mei, Q. Jing, X. Zou, L. Wang, Q. Xu, L. Yang and H. Guo, *ACS Sustainable Chem. Eng.*, 2023, **11**, 7263-7273.

49. Z. Yang, K. Jiang, G. Tong, C. Ke, H. Wu, P. Liu, J. Zhang, H. Ji, J. Zhu and C. Lu, *Chem. Eng. J.*, 2022, **437**, 135377.

50. L. Wu, Y. Chen, C. Shao, L. Wang and B. Li, *Adv. Funct. Mater.*, 2024, **34**, 2408257.

51. W. Guo, M. Pan, Q. Xie, H. Fan, L. Luo, Q. Jing, Y. Shen, Y. Yan, M. Liu and Z. Wang, *Nat. Commun.*, 2025, **16**, 1-13.

52. Y. Qi, W. Shan, H. Yu, J. Cui, Z. Lou, X. Feng and Y. Xiong, *Chem. Eng. J.*, 2025, 161543.

53. L. Yan, L. Xie, X. L. Wu, M. Qian, J. Chen, Y. Zhong and Y. Hu, *Carbon Energy*, 2021, **3**, 856-865.